

1

2 The ANTsX ecosystem for mapping the mouse 3 brain

4 Nicholas J. Tustison^{1,✉}, Min Chen², Fae N. Kronman³, Jeffrey T. Duda², Clare Gamlin⁴,
5 Mia G. Tustison⁵, Michael Kunst⁴, Rachel Dalley⁴, Staci Sorenson⁴, Quanxin Wang⁴, Lydia
6 Ng⁴, Yongsoo Kim³, and James C. Gee^{2,✉}

7 ¹Department of Radiology and Medical Imaging, University of Virginia, Charlottesville, VA

8 ²Department of Radiology, University of Pennsylvania, Philadelphia, PA

9 ³Department of Neuroscience and Experimental Therapeutics, Penn State University, Hershey, PA

10 ⁴Allen Institute for Brain Science, Seattle, WA

11 ⁵Santiago High School, Corona, CA

12

13 ✉ Corresponding authors:

14

15 Nicholas J. Tustison, DSc

16 Department of Radiology and Medical Imaging

17 University of Virginia

18 ntustison@virginia.edu

19

20 James C. Gee, PhD

21 Department of Radiology

22 University of Pennsylvania

23 gee@upenn.edu

²⁴ **Abstract**

²⁵ Large-scale efforts by the BRAIN Initiative Cell Census Network (BICCN) are generating
²⁶ a comprehensive reference atlas of cell types in the mouse brain. A key challenge in this
²⁷ effort is mapping diverse datasets, acquired with varied imaging, tissue processing, and
²⁸ profiling methods, into shared coordinate frameworks. Here, we present modular mapping
²⁹ pipelines developed using the Advanced Normalization Tools Ecosystem (ANTsX) to align
³⁰ MERFISH spatial transcriptomics and high-resolution fMOST morphology data to the Allen
³¹ Common Coordinate Framework (CCFv3), and developmental MRI and LSFM data to the
³² Developmental CCF (DevCCF). Simultaneously, we introduce two novel methods: 1) a
³³ velocity field-based approach for continuous interpolation across developmental timepoints,
³⁴ and 2) a deep learning framework for automated brain parcellation using minimally annotated
³⁵ and publicly available data. All workflows are open-source and reproducible. We also provide
³⁶ general guidance for selecting appropriate strategies across modalities, enabling researchers
³⁷ to adapt these tools to new data.

³⁸ 1 Introduction

³⁹ Over the past decade, there have been significant advancements in mesoscopic single-cell
⁴⁰ analysis of the mouse brain. It is now possible to track single neurons¹, observe whole-
⁴¹ brain developmental changes at cellular resolution², associate brain regions with genetic
⁴² composition³, and locally characterize neural connectivity⁴. These scientific achievements have
⁴³ been propelled by high-resolution profiling and imaging techniques that enable submicron,
⁴⁴ multimodal, 3D characterizations of whole mouse brains. Among these are micro-optical
⁴⁵ sectioning tomography^{5,6}, tissue clearing methods^{1,7}, spatial transcriptomics^{8,9}, and single-cell
⁴⁶ genomic profiling¹⁰, each offering expanded specificity and resolution for cell-level brain
⁴⁷ analysis.

⁴⁸ Recent efforts by the NIH BRAIN Initiative have mobilized large-scale international col-
⁴⁹ laborations to create a comprehensive reference database of mouse brain structure and
⁵⁰ function. The BRAIN Initiative Cell Census Network has aggregated over 40 multimodal
⁵¹ datasets from more than 30 research groups¹¹, many of which are registered to standardized
⁵² anatomical coordinate systems to support integrated analysis. Among the most widely used
⁵³ of these frameworks is the Allen Mouse Brain Common Coordinate Framework (CCFv3)¹².
⁵⁴ Other CCFs include modality-specific references^{13–15} and developmental atlases^{16,17} that track
⁵⁵ structural change across time.

⁵⁶ 1.1 Mouse brain mapping challenges

⁵⁷ Robust mapping of cell type data into CCFs is essential for integrative analysis of morphology,
⁵⁸ connectivity, and molecular identity. However, each modality poses unique challenges. For
⁵⁹ example, differences in tissue processing, imaging protocols, and anatomical completeness
⁶⁰ often introduce artifacts such as distortion, tearing, holes, and signal dropout^{18–23}. Intensity
⁶¹ differences and partial representations of anatomy can further complicate alignment. Also,
⁶² while alternative strategies for mapping single-cell spatial transcriptomic data exist (e.g., gene
⁶³ expression-based models such as Tangram²⁴) this work focuses on image-based anatomical
⁶⁴ alignment to common coordinate frameworks using spatially resolved reference images. Given

65 this diversity specialized strategies are often needed to address the unique, modality-specific
66 challenges.

67 Existing mapping solutions fall into three broad categories. The first includes integrated
68 processing platforms that provide users with mapped datasets (e.g., Allen Brain Cell Atlas²⁵,
69 Brain Architecture Portal²⁶, OpenBrainMap²⁷, and Image and Multi-Morphology Pipeline²⁸).
70 These offer convenience and high-quality curated data, but limited generalizability and
71 customization. The second category involves highly specialized pipelines tailored to specific
72 modalities such as histology^{29–31}, magnetic resonance imaging (MRI)^{32–34}, microCT^{35,36}, light
73 sheet fluorescence microscopy (LSFM)^{37,38}, fluorescence micro-optical sectioning tomography
74 (fMOST)^{15,39}, and spatial transcriptomics, including multiplexed error-robust fluorescence in
75 situ hybridization (MERFISH)^{40–42}. While effective, these solutions often require extensive
76 engineering effort to adapt to new datasets or modalities. Finally, general-purpose toolkits
77 such as elastix⁴³, Slicer3D⁴⁴, and the Advanced Normalization Tools Ecosystem (ANTsX)⁴⁵
78 have all been applied to mouse brain mapping scenarios. These toolkits support modular
79 workflows that can be flexibly composed from reusable components, offering a powerful
80 alternative to rigid, modality-specific solutions. However, their use often requires familiarity
81 with pipeline modules, parameter tuning, and tool-specific conventions which can limit
82 adoption.

83 Building on this third category, we describe a set of modular, ANTsX-based pipelines
84 specifically tailored for mapping diverse mouse brain data into standardized anatomical
85 frameworks. These include two new pipelines: a velocity field-based interpolation model that
86 enables continuous transformations across developmental timepoints of the DevCCF, and a
87 template-based deep learning pipeline for whole brain segmentation (i.e., brain extraction)
88 and structural anatomical regional labeling of the brain (i.e., brain parcellation) requiring
89 minimal annotated data. In addition, we include two modular pipelines for aligning MERFISH
90 and fMOST datasets to the Allen CCFv3. While the MERFISH dataset was previously
91 published as part of earlier BICCN efforts⁴⁶, the full image processing and registration
92 workflow had not been described in detail until now. The fMOST workflow, by contrast,
93 was developed internally to support high-resolution morphology mapping and has not been

94 previously published in any form. Both pipelines were built using ANTsX tools, adapted
95 for collaborative use with the Allen Institute, and are now released as fully reproducible,
96 open-source workflows to support reuse and extension by the community. To facilitate broader
97 adoption, we also provide general guidance for customizing these strategies across imaging
98 modalities and data types. We first introduce key components of the ANTsX toolkit, which
99 provide a basis for all of the mapping workflows described here, and then detail the specific
100 contributions made in each pipeline.

101 1.2 The Advanced Normalization Tools Ecosystem (ANTsX)

102 The Advanced Normalization Tools Ecosystem (ANTsX) has been used in a number of
103 applications for mapping mouse brain data as part of core processing steps in various
104 workflows^{31,46–49}, particularly its pairwise, intensity-based image registration capabilities⁵⁰
105 and bias field correction⁵¹. Historically, ANTsX development is based on foundational
106 approaches to image mapping^{52–54}, especially in the human brain, with key contributions such
107 as the Symmetric Normalization (SyN) algorithm⁵⁰. It has been independently evaluated in
108 diverse imaging domains including multi-site brain MRI⁵⁵, pulmonary CT⁵⁶, and multi-modal
109 brain tumor registration⁵⁷. More recent contributions for mouse-specific applications showcase
110 multimodal template generation¹⁶ and anatomy-aware registration ANTsX functionality.

111 Beyond registration, ANTsX provides functionality for template generation⁵⁸, segmentation⁵⁹,
112 preprocessing^{51,60}, and deep learning⁴⁵. It has demonstrated strong performance in consensus
113 labeling⁶¹, brain tumor segmentation⁶², and cardiac motion estimation⁶³. Built on the
114 Insight Toolkit (ITK)⁶⁴, ANTsX benefits from open-source contributions while supporting
115 continued algorithm evaluation and innovation. In the context of mouse brain data, ANTsX
116 provides a robust platform for developing modular pipelines to map diverse imaging modalities
117 into CCFs. These tools span multiple classes of mapping problems: cross-modality image
118 registration, landmark-driven alignment, temporal interpolation across developmental stages,
119 and deep learning-based segmentation. As such, they also serve as illustrative case studies
120 for adapting ANTsX tools to other use cases. We describe both shared infrastructure and
121 targeted strategies adapted to the specific challenges of each modality. This paper highlights

122 usage across distinct BICCN projects such as spatial transcriptomic data from MERFISH,
123 structural data from fMOST, and multimodal developmental data from LSFM and MRI.

124 1.3 Novel ANTsX-based open-source contributions

125 We introduce two novel contributions to ANTsX developed as part of collabortive efforts in
126 creating the Developmental Common Coordinate Framework (DevCCF)¹⁶. First, we present
127 an open-source velocity field–based interpolation framework for continuous mapping across the
128 sampled embryonic and postnatal stages of the DevCCF atlas¹⁶. This functionality enables
129 biologically plausible interpolation between timepoints via a time-parameterized diffeomorphic
130 velocity model⁶⁵, inspired by previous work⁶⁶. Second, we present a deep learning pipeline for
131 structural parcellation of the mouse brain from multimodal MRI data. This includes two novel
132 components: 1) a template-derived brain extraction model using augmented data from two
133 ANTsX-derived template datasets^{67,68}, and 2) a template-derived parcellation model trained
134 on DevCCF P56 labelings mapped from the AllenCCFv3. This pipeline demonstrates how
135 ANTsX tools and public resources can be leveraged to build robust anatomical segmentation
136 pipelines with minimal annotated data. We independently evaluate this framework using a
137 longitudinal external dataset⁶⁹, demonstrating generalizability across specimens and imaging
138 protocols. All components are openly available through the R and Python ANTsX packages,
139 with general-purpose functionality documented in a reproducible, cross-platform tutorial
140 (<https://tinyurl.com/antsxtutorial>). Code specific to this manuscript, including scripts to
141 reproduce the novel contributions and all associated evaluations, is provided in a dedicated
142 repository (<https://github.com/ntustison/ANTsXMouseBrainMapping>). Additional tools for
143 mapping spatial transcriptomic (MERFISH) and structural (fMOST) data to the AllenCCFv3
144 are separately available at (<https://github.com/dontminchenit/CCFAlignmentToolkit>).

2 Results

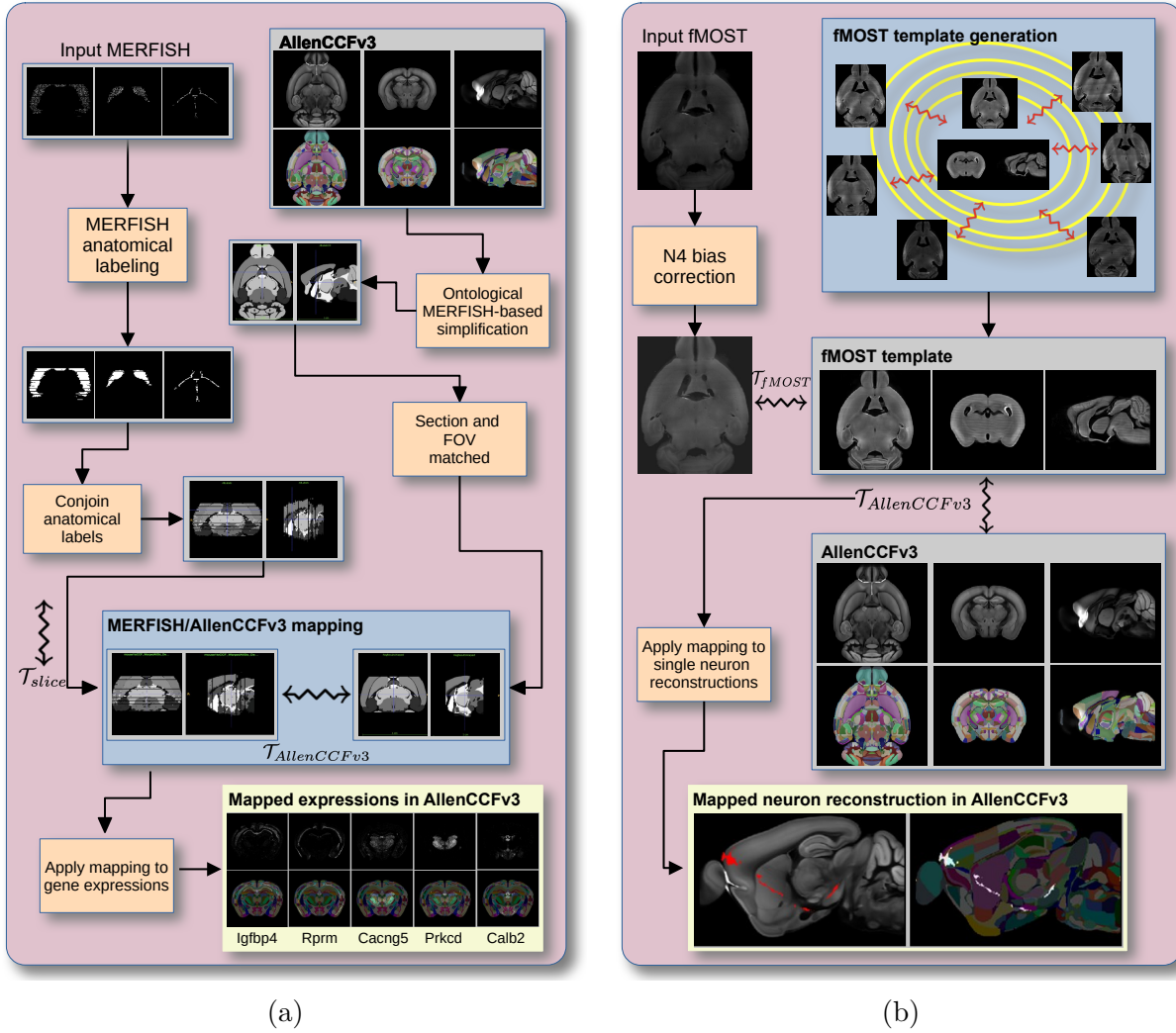


Figure 1: Diagram of the two ANTsX-based pipelines for mapping (a) MERFISH and (b)fMOST data into the space of AllenCCFv3. Each generates the requisite transforms to map individual images to the CCF.

2.1 Mapping multiplexed error-robust fluorescence *in situ* hybridization (MERFISH)

We developed an ANTsX-based pipeline to map spatial transcriptomic MERFISH data into the AllenCCFv3 (Figure 1(a)). This approach was used in recent efforts to create a high-resolution transcriptomic atlas of the mouse brain⁴⁶. The pipeline maps spatial gene

151 expression patterns from MERFISH onto anatomical labels in the AllenCCFv3. It includes
152 MERFISH-specific preprocessing steps such as section reconstruction, label generation from
153 spatial transcriptomic maps, and anatomical correspondence mapping. Alignment proceeds
154 in two stages: 1) 3D affine registration and section matching of the AllenCCFv3 to the
155 MERFISH data, and 2) linear + deformable 2D section-wise alignment between matched
156 MERFISH and atlas slices. These transformations are concatenated to produce a complete
157 mapping from each MERFISH data to AllenCCFv3.

158 MERFISH imaging was performed on cryosectioned brains from C57BL/6 mice using previ-
159 ously described protocols⁴⁶. Brains were placed into an optimal cutting temperature (OCT)
160 compound (Sakura FineTek 4583) stored at -80°. The fresh frozen brain was sectioned at 10
161 μm on Leica 3050 S cryostats at intervals of 200 μm to evenly cover the brain. A set of 500
162 genes was selected to distinguish \sim 5200 transcriptomic clusters. Raw MERSCOPE data were
163 decoded using Vizgen software (v231). Cell segmentation was performed using Cellpose^{70,71}
164 based on DAPI and PolyT stains which was propagated to adjacent slices across z-planes.
165 Each MERFISH cell was assigned a transcriptomic identity by mapping to a scRNA-seq
166 reference taxonomy.

167 Alignment quality was evaluated iteratively by an expert anatomist, guided by expected
168 gene-marker correspondences to AllenCCFv3 regions. As previously reported⁴⁶, further
169 assessment of the alignment showed that, of the 554 terminal regions (gray matter only in
170 the AllenCCFv3), only seven small subregions did not contain cells from the MERFISH
171 dataset post registration: frontal pole, layer 1 (FRP1), FRP2/3, FRP5; accessory olfactory
172 bulb, glomerular layer (AOBgl); accessory olfactory bulb, granular layer (AOBgr); accessory
173 olfactory bulb, mitral layer (AOBmi); and accessory supraoptic group (ASO). A broader
174 discussion of evaluation design choices and evaluation rationale is included in the Discussion.

¹⁷⁵ **2.2 Mapping fluorescence micro-optical sectioning tomography**
¹⁷⁶ **(fMOST) data**

¹⁷⁷ We also constructed a pipeline for mapping fMOST images to the AllenCCFv3 using ANTsX
¹⁷⁸ (Figure 1(b)). The approach leverages a modality-specific average fMOST atlas as an interme-
¹⁷⁹ diate target, adapted from previous work in human and mouse brain mapping^{12,15,16,58,72–75}.

¹⁸⁰ The atlas was constructed from 30 fMOST images selected to capture representative variability
¹⁸¹ in anatomical shape and image intensity across the population. Preprocessing includes cubic
¹⁸² B-spline downsampling to match the 25 μm isotropic AllenCCFv3 resolution, stripe artifact
¹⁸³ suppression using a 3D notch filter implemented with SciPy’s frequency-domain filtering
¹⁸⁴ tools, and N4 bias field correction⁵¹. A one-time, annotation-driven alignment registers
¹⁸⁵ the fMOST atlas to AllenCCFv3 using landmark-based registration of key structures. This
¹⁸⁶ canonical mapping is then reused. New fMOST specimens are first aligned to the fMOST
¹⁸⁷ atlas using standard intensity-based registration, and the concatenated transforms yield full
¹⁸⁸ spatial normalization to the AllenCCFv3. This same mapping can be applied to neuron
¹⁸⁹ reconstructions to facilitate population-level analysis of morphology and spatial distribution.

¹⁹⁰ fMOST imaging was performed on 55 mouse brains with sparse transgenic labeling of
¹⁹¹ neuron populations^{76,77} using the high-throughput fMOST platform^{78,79}. Voxel resolution was
¹⁹² $0.35 \times 0.35 \times 1.0 \mu\text{m}^3$. Two imaging channels were acquired: GFP-labeled neuron morphology
¹⁹³ (green), and propidium iodide counterstaining for cytoarchitecture (red). Alignment was
¹⁹⁴ performed using the red channel for its greater contrast, though multi-channel mapping is
¹⁹⁵ also supported.

¹⁹⁶ The canonical mapping from the fMOST atlas to AllenCCFv3 was evaluated using both
¹⁹⁷ quantitative and qualitative approaches. Dice similarity coefficients were computed between
¹⁹⁸ corresponding anatomical labels in the fMOST atlas and AllenCCFv3 following registra-
¹⁹⁹ tion. These labels were manually annotated or adapted from existing atlas segmentations.
²⁰⁰ Representative Dice scores included: whole brain (0.99), caudate putamen (0.97), fimbria
²⁰¹ (0.91), posterior choroid plexus (0.93), anterior choroid plexus (0.96), optic chiasm (0.77), and
²⁰² habenular commissure (0.63). In addition to these quantitative assessments, each registered
²⁰³ fMOST specimen was evaluated qualitatively. An expert anatomist reviewed alignment

accuracy and confirmed structural correspondence. Neuron reconstructions from individual brains were also transformed into AllenCCFv3 space, and their trajectories were visually inspected to confirm anatomical plausibility and preservation of known projection patterns. A broader discussion of evaluation design choices and evaluation rationale is included in the Discussion.

2.3 Continuously mapping the DevCCF developmental trajectory

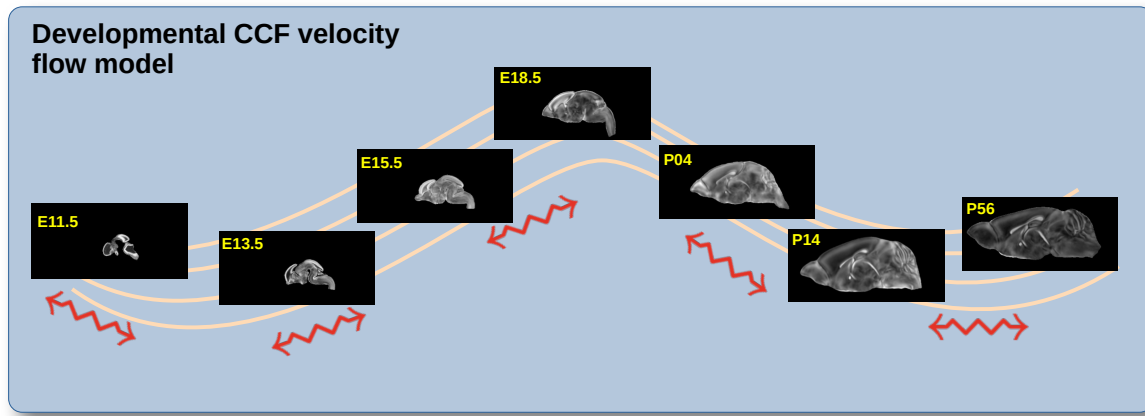


Figure 2: The spatial transformation between any two time points within the continuous DevCCF longitudinal developmental trajectory is available through the use of ANTsX functionality for generating a velocity flow model.

The DevCCF is an openly accessible resource for the mouse brain research community¹⁶, comprising symmetric, multi-modal MRI and LSFM templates generated using the ANTsX framework⁵⁸. It spans key stages of mouse brain development (E11.5, E13.5, E15.5, E18.5, P4, P14, and P56) and includes structural labels defined by a developmental ontology. The DevCCF was constructed in coordination with the AllenCCFv3 to facilitate integration across atlases and data types.

Although this collection provides broad developmental coverage, its discrete sampling limits the ability to model continuous transformations across time. To address this, we developed a velocity flow-based modeling approach that enables anatomically plausible, diffeomorphic transformations between any two continuous time points within the DevCCF range. Unlike traditional

220 pairwise interpolation, which requires sequential warping through each intermediate stage, this
 221 model, defined by a time-varying velocity field (i.e., a smooth vector field defined over space
 222 and time that governs the continuous deformation of an image domain), allows direct computa-
 223 tion of deformations between any two time points in the continuum which improves smoothness
 224 and enables flexible spatiotemporal alignment. This functionality is implemented in both
 225 ANTsR and ANTsPy (see `ants.fit_time_varying_transform_to_point_sets(...)`) and
 226 integrates seamlessly with existing ANTsX workflows. The velocity field is represented
 227 as a 4D ITK image where each voxel stores the x,y,z components of motion at a given
 228 time point. Integration of the time-varying velocity field uses uses 4th order Runge-Kutta
 229 (`ants.integrate_velocity_field(...)`)⁸⁰.

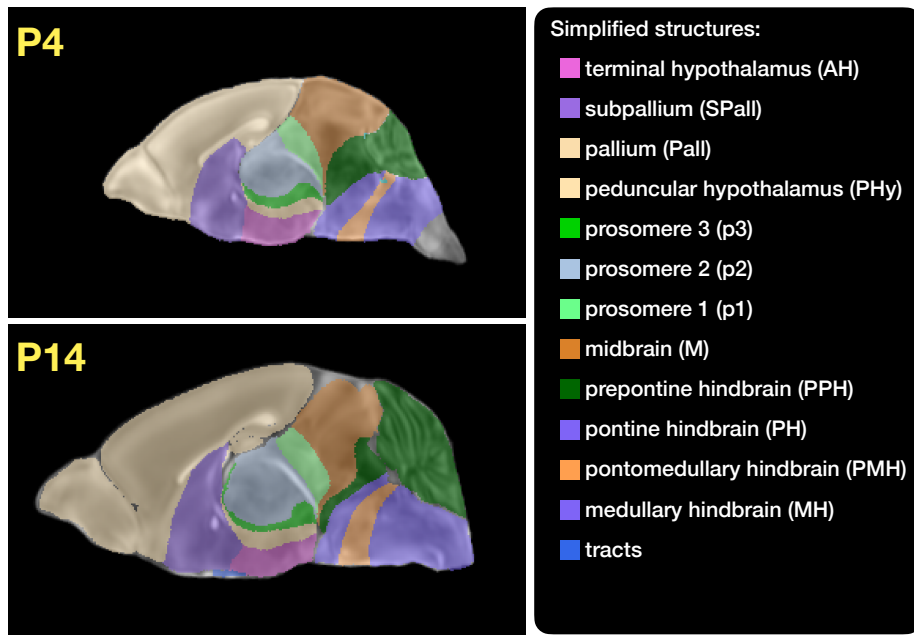


Figure 3: Annotated regions representing common labels across developmental stages, shown for both P4 and P14.

230 Each DevCCF template includes over 2,500 labeled anatomical regions, with spatial resolutions
 231 ranging from 31.5 to 50 μ m. For the velocity flow modeling task, we identified a common set
 232 of 26 bilateral regions (13 per hemisphere) that were consistently labeled across all timepoints.
 233 These regions span major developmental domains including the pallium, subpallium, midbrain,
 234 prosomeres, hypothalamus, hindbrain subregions, and key white matter tracts (Figure 3).
 235 Prior to velocity field optimization, all templates were rigidly aligned to the DevCCF

236 P56 template using the centroids of these common label sets. Pairwise correspondence
237 between adjacent timepoints was then computed using ANTsX’s multi-metric registration
238 via `ants.registration(...)`. Instead of performing intensity-based multi-label registration
239 directly, we constructed 24 binary label masks per atlas pair (one per structure) and optimized
240 alignment using the mean squares similarity metric with the SyN transform⁵⁰.

241 To generate the point sets for velocity field optimization, we sampled both boundary (contour)
242 and interior (region) points from the P56 labels and propagated them to each developmental
243 stage using the learned pairwise transforms. Contours were sampled at 10% of available points
244 and regions at 1%, yielding 173,303 total points per atlas ($N_{contour} = 98,151$; $N_{region} = 75,152$).
245 Boundary points were assigned double weight during optimization to emphasize anatomical
246 boundary correspondence.

247 The velocity field was optimized using the seven corresponding point sets and their associated
248 weights. The field geometry was defined at [256, 182, 360] with 11 integration points at 50
249 μm resolution, yielding a compressed velocity model of ~ 2 GB. This resolution balanced
250 accuracy and computational tractability while remaining portable. All data and code are
251 publicly available in the accompanying GitHub repository.

252 To normalize temporal spacing, we assigned scalar values in [0, 1] to each template. Given
253 the nonlinear spacing in postnatal development, we applied a logarithmic transform to the
254 raw time values prior to normalization. Within this logarithmic temporal transform, P56 was
255 assigned a span of 28 postnatal days to reflect known developmental dynamics (i.e., in terms
256 of modeling the continuous deformation, the morphological changes between Day 28 and Day
257 56 are insignificant). This improved the temporal distribution of integration points (Figure 4,
258 right panel).

259 Optimization was run for a maximum of 200 iterations using a 2020 iMac (3.6 GHz 10-Core
260 Intel Core i9, 64 GB RAM), with each iteration taking ~ 6 minutes. During each iteration,
261 the velocity field was updated across all 11 integration points by computing regularized
262 displacement fields between warped point sets at adjacent time slices. Updates were applied
263 using a step size of $\delta = 0.2$. Convergence was assessed via average displacement error
264 across all points, with final convergence achieved after ~ 125 iterations (Figure 4, left panel).

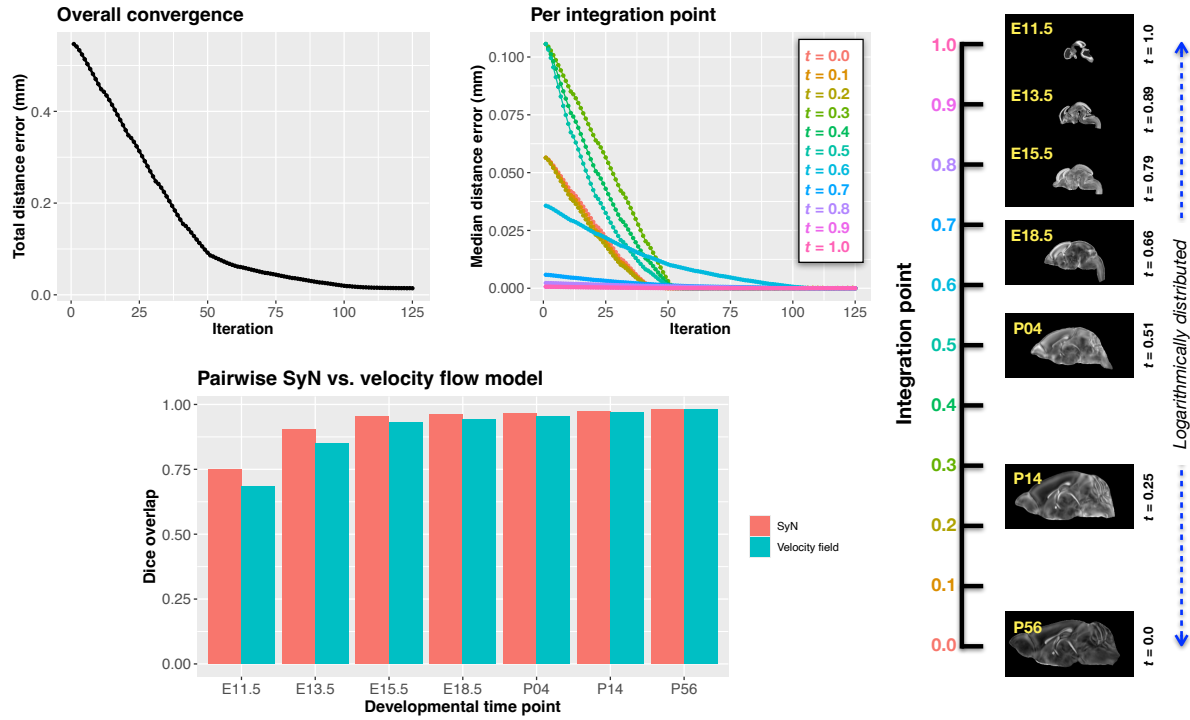


Figure 4: Convergence and evaluation of the velocity flow model across the DevCCF developmental trajectory. (Top left) Total displacement error over iterations. (Top right) Median displacement error per integration point across the optimization timeline, spanning embryonic (E11.5) to postnatal (P56) stages. (Bottom) Dice similarity scores comparing region-level label overlap between: (1) conventional pairwise SyN registration and (2) velocity flow-based deformation, across intermediate timepoints. Using region-based pairwise registration with SyN as a performance upper bound, the velocity flow model achieves comparable accuracy while also enabling smooth, continuous deformation across the full developmental continuum.

265 Median errors across integration points also trended toward zero, albeit at varying rates.
 266 To benchmark performance, we compared the velocity model’s region-based alignment to
 267 traditional pairwise registration using SyN, a widely used diffeomorphic algorithm. The
 268 velocity model achieved comparable Dice scores at sampled timepoints while additionally
 269 offering smooth interpolation across the entire developmental trajectory.
 270 Once optimized, the velocity field enables the computation of diffeomorphic transformations
 271 between any pair of continuous time points within the DevCCF developmental range. Figure 5
 272 illustrates cross-warping between all DevCCF stages using the velocity flow model. In addition
 273 to facilitating flexible alignment between existing templates, the model also supports the
 274 synthesis of virtual templates at intermediate, unsampled developmental stages. As shown

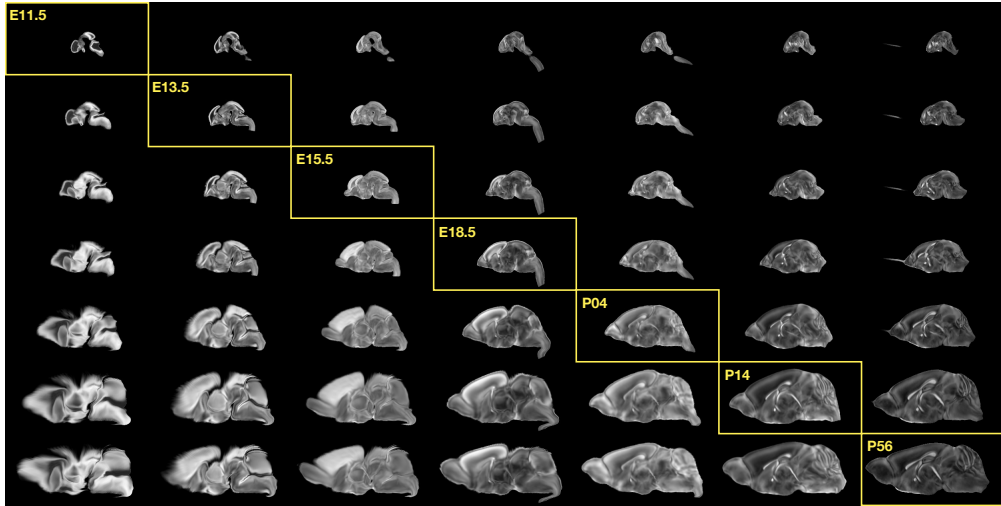


Figure 5: Mid-sagittal visualization of DevCCF templates warped to every other time point. Each row is a reference space; each column is a warped input. Diagonal entries show original templates.

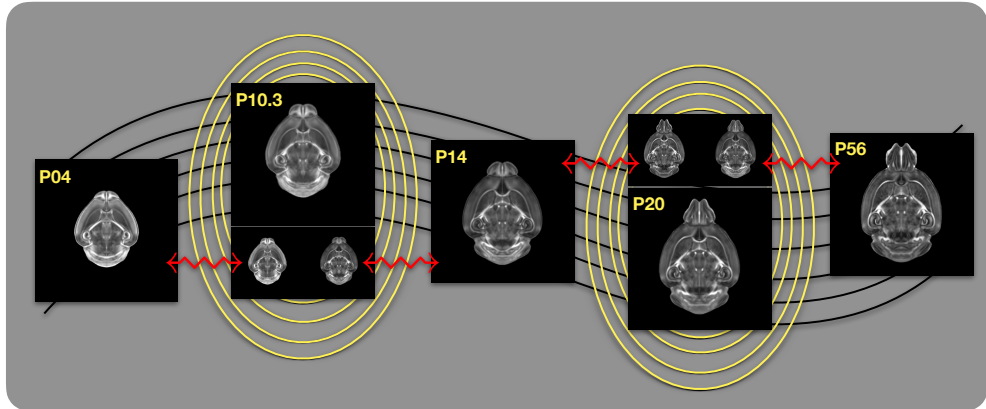


Figure 6: Example of generating “virtual” DevCCF templates at intermediate time points (e.g., P10.3, P20) by warping adjacent developmental atlases to a target timepoint and averaging using ANTsX.

275 in Figure 6, we demonstrate the creation of virtual age templates (e.g., P10.3 and P20) by
 276 warping adjacent developmental atlases to a target timepoint and constructing an averaged
 277 representation using ANTsX’s template-building functionality.
 278 All usage examples, scripts, and supporting data for full reproducibility are publicly available
 279 in the associated codebase.

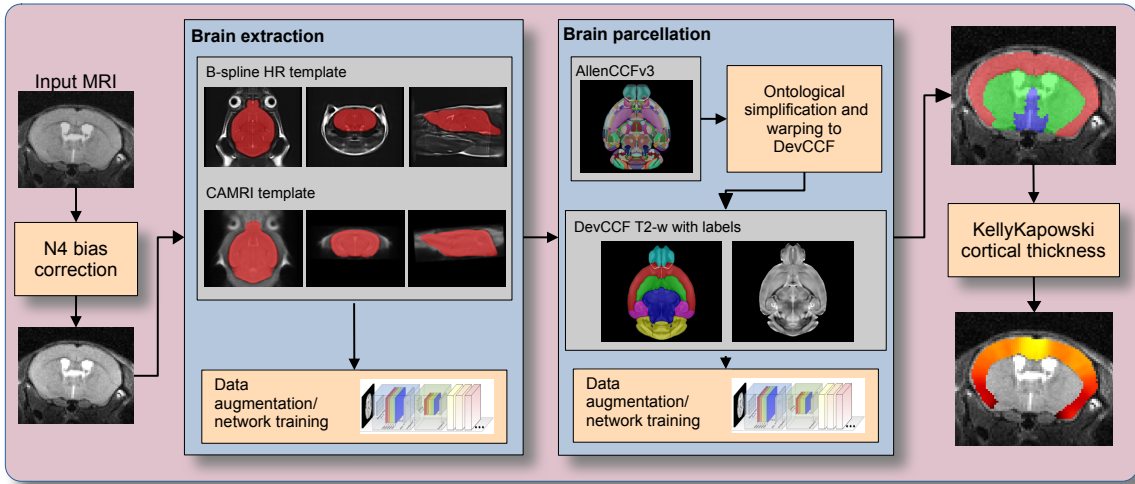


Figure 7: The mouse brain cortical labeling pipeline integrates two deep learning components for brain extraction and anatomical region segmentation. Both networks rely heavily on data augmentation applied to templates constructed from open datasets. The framework also supports further refinement or alternative label sets tailored to specific research needs. Possible applications include voxelwise cortical thickness estimation.

280 2.4 Automated structural labeling of the mouse brain

281 Structural labeling strategies for the mouse brain are essential for understanding the organization
 282 and function of the murine nervous system⁸¹. By dividing the brain into anatomically
 283 or functionally defined regions, researchers can localize biological processes, relate regional
 284 features to behavior, or quantify spatial variation in gene expression patterns^{82,83}. While deep
 285 learning techniques have yielded robust segmentation and labeling tools for the human brain
 286 (e.g., SynthSeg⁸⁴, ANTsXNet⁴⁵), analogous development for mouse data (e.g., MEMOS⁸⁵)
 287 has been limited. Mouse neuroimaging often presents unique challenges, such as highly
 288 anisotropic sampling, that complicate transfer of existing tools. At the same time, high
 289 resolution resources like the AllenCCFv3 and DevCCF provide reference label sets that can
 290 serve as training data. We demonstrate how ANTsX can be used to construct a full structural
 291 labeling pipeline for the mouse brain (Figure 7), including both whole brain segmentation
 292 (i.e., brain extraction) and the subsequent template-based region segmentation.

293 To develop a general-purpose mouse brain extraction model, we constructed whole-head
 294 templates from two publicly available T2-weighted datasets. The first dataset, from the

295 Center for Animal MRI (CAMRI) at the University of North Carolina at Chapel Hill⁶⁷,
296 includes 16 isotropic MRI volumes acquired at $0.16 \times 0.16 \times 0.16$ mm³ resolution. The
297 second dataset⁶⁸ comprises 88 specimens acquired in three orthogonal 2D views (coronal,
298 axial, sagittal) at 0.08×0.08 mm³ in-plane resolution with 0.5 mm slice thickness. These
299 orthogonal 2D acquisitions were reconstructed into high-resolution 3D volumes using a B-
300 spline fitting algorithm⁸⁶. Using this synthesized dataset and the CAMRI images, we created
301 two ANTsX-based population templates⁵⁸, each paired with a manually delineated brain mask.
302 These served as the basis for training an initial template-based brain extraction model. Deep
303 learning training of the network employed aggressive data augmentation strategies, including
304 bias field simulation, histogram warping, random spatial deformation, noise injection, and
305 anisotropic resampling. This enabled the model to generalize beyond the two templates. The
306 initial model was released through ANTsXNet and made publicly available.

307 Subsequent community use led to further improvements. A research group applying the
308 tool to their own ex vivo T2-weighted mouse brain data contributed a third template and
309 associated mask (acquired at 0.08 mm isotropic resolution). Incorporating this into the
310 training data improved robustness and accuracy to an independent dataset and extended
311 the model's generalizability. The refined model is distributed through ANTsPyNet via
312 `antspynet.mouse_brain_extraction(...)`.

313 The AllenCCFv3 atlas and its hierarchical ontology, along with the DevCCF, provide a strong
314 foundation for developing region-wise anatomical labeling models for multi-modal mouse
315 brain imaging. Using the `allensdk` Python library, we generated a coarse segmentation
316 scheme by grouping anatomical labels into six major regions: cerebral cortex, cerebral nuclei,
317 brainstem, cerebellum, main olfactory bulb, and hippocampal formation. These labels were
318 mapped onto the P56 T2-weighted DevCCF template to serve as training targets. We trained
319 a 3D U-net-based segmentation network using this template and the same augmentation
320 strategies described for brain extraction. The model is publicly available via ANTsXNet
321 (`antspynet.mouse_brain_parcellation(...)`) and supports robust anatomical labeling
322 across diverse imaging geometries and contrasts. The inclusion of aggressive augmentation,
323 including simulated anisotropy, enables the model to perform well even on thick-slice input

324 data. Internally, the model reconstructs isotropic probability and label maps, facilitating
325 downstream morphometric analyses. For example, this network integrates with the ANTsX
326 cortical thickness estimation pipeline (`antspynet.mouse_cortical_thickness(...)`) to
327 produce voxelwise cortical thickness maps, even when applied to anisotropic or limited-
328 resolution mouse brain data.

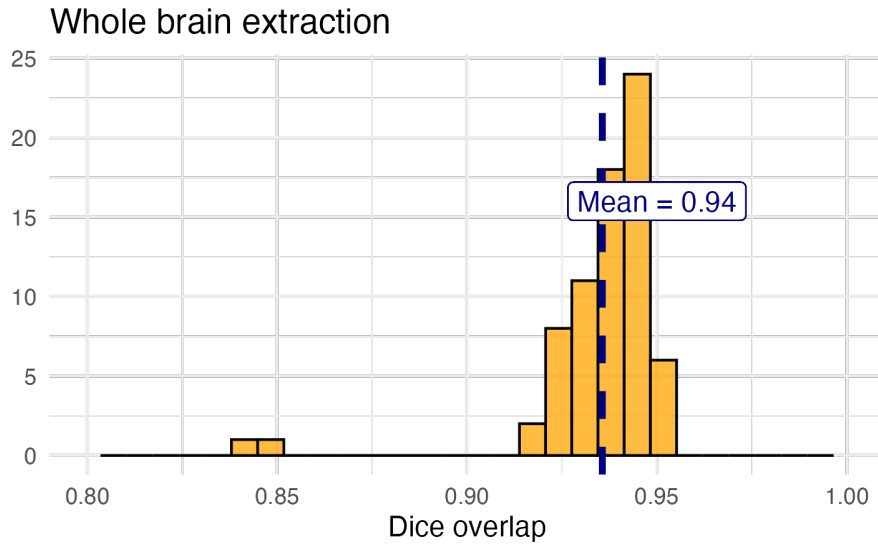
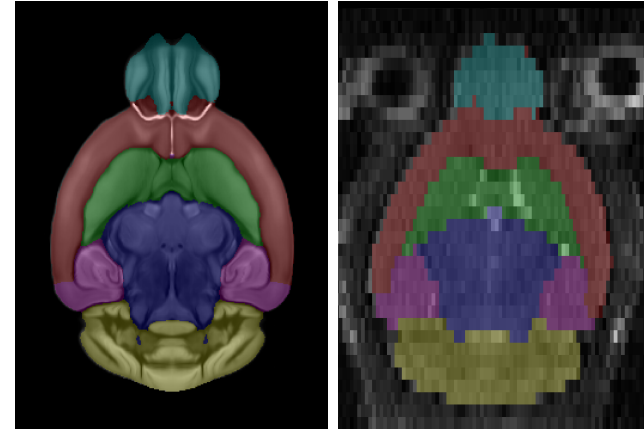


Figure 8: Evaluation of the ANTsX mouse brain extraction on an independent, publicly available dataset consisting of 12 specimens \times 7 time points = 84 total images. Dice overlap comparisons with the user-generated brain masks provide good agreement with the automated results from the brain extraction network.

329 For evaluation, we used an additional publicly available dataset⁶⁹ that is completely indepen-
330 dent from the data used in training the brain extraction and parcellation networks. Data
331 includes 12 specimens each imaged at seven time points (Day 0, Day 3, Week 1, Week 4,
332 Week 8, Week 20) with in-house-generated brain masks (i.e., produced by the data providers)
333 for a total of 84 images. Spacing is anistropic with an in-plane resolution of $0.1 \times 0.1 \text{ mm}^2$
334 and a slice thickness of 0.5 mm.

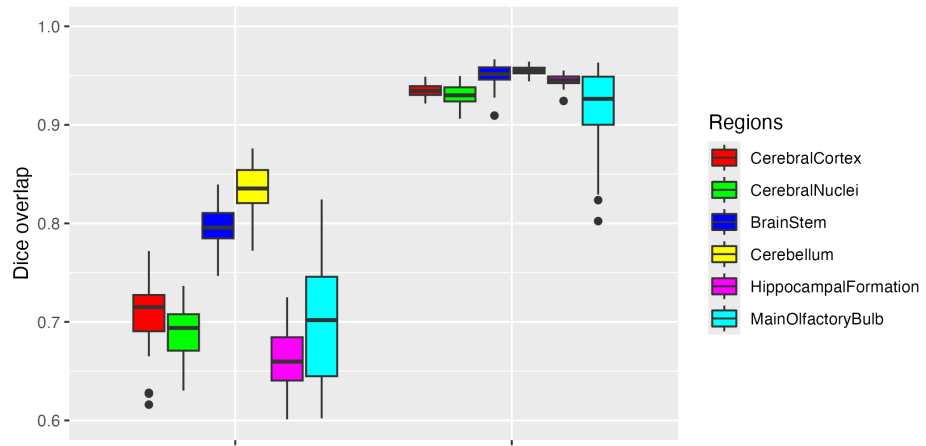
335 Figure 8 summarizes the whole-brain overlap between manually segmented reference masks
336 and the predicted segmentations for all 84 images in the evaluation cohort. The proposed
337 network demonstrates excellent performance in brain extraction across a wide age range. To
338 further assess the utility of the parcellation network, we used the predicted labels to guide
339 anatomically informed registration to the AllenCCFv3 atlas using ANTsX multi-component



(a)

(b)

Normalization to AllenCCFv3



(c)

Figure 9: Evaluation of the ANTsX deep learning–based mouse brain parcellation on a diverse MRI cohort. (a) T2-weighted DevCCF P56 template with the six-region parcellation: cerebral cortex, nuclei, brain stem, cerebellum, main olfactory bulb, and hippocampal formation. (b) Example segmentation result from a representative subject (NR5, Day 0) using the proposed deep learning pipeline. (c) Dice overlap scores across the full evaluation cohort ($n = 84$), comparing anatomical alignment achieved via registration using intensity alone versus registration guided by the predicted parcellation. Dice values were computed using manually segmented labels transformed to AllenCCFv3 space.

³⁴⁰ registration, and compared this to intensity-only registration (Figure 9). While intensity-based
³⁴¹ alignment performs reasonably well, incorporating the predicted parcellation significantly
³⁴² improves regional correspondence. Dice scores shown in Figure 9(c) were computed using
³⁴³ manually segmented labels transformed to AllenCCFv3 space.

³⁴⁴ **3 Discussion**

³⁴⁵ The diverse mouse brain cell type profiles gathered through BICCN and associated efforts
³⁴⁶ provide a rich multi-modal resource to the research community. However, despite significant
³⁴⁷ progress, optimal leveraging of these valuable resources remains an ongoing challenge. A
³⁴⁸ central component to data integration is accurately mapping novel cell type data into
³⁴⁹ common coordinate frameworks (CCFs) for subsequent processing and analysis. To meet
³⁵⁰ these needs, tools for mapping mouse brain data must be both broadly accessible and
³⁵¹ capable of addressing challenges unique to each modality. In this work, we described modular
³⁵² ANTsX-based pipelines developed to support three distinct BICCN efforts encompassing
³⁵³ spatial transcriptomic, morphological, and developmental data. We demonstrated how a
³⁵⁴ flexible image analysis toolkit like ANTsX can be tailored to address specific modality-driven
³⁵⁵ constraints by leveraging reusable, validated components.

³⁵⁶ As part of collaborative efforts with the Allen Institute for Brain Science and the broader
³⁵⁷ BICCN initiative, we developed two modular pipelines for mapping MERFISH and fMOST
³⁵⁸ datasets to the AllenCCFv3. These workflows were designed to accommodate the specific
³⁵⁹ requirements of high-resolution transcriptomic and morphological data while leveraging
³⁶⁰ reusable components from the ANTsX ecosystem. The MERFISH pipeline incorporates
³⁶¹ preprocessing and registration steps tailored to known anatomical and imaging artifacts in
³⁶² multiplexed spatial transcriptomic data. While the general mapping strategy is applicable
³⁶³ to other sectioned histological datasets, these refinements demonstrate how general-purpose
³⁶⁴ tools can be customized to meet the demands of specialized modalities. The fMOST workflow,
³⁶⁵ in contrast, emphasizes reusability and consistency across large datasets. It introduces an
³⁶⁶ intermediate, canonical fMOST atlas to stabilize transformations to the AllenCCFv3, reducing
³⁶⁷ the need for repeated manual alignment and enabling standardized mapping of single-neuron
³⁶⁸ reconstructions to a common coordinate framework.

³⁶⁹ Evaluation of both workflows followed established QA/QC protocols used at the Allen
³⁷⁰ Institute, emphasizing biologically meaningful criteria such as expected gene-marker alignment
³⁷¹ (MERFISH) and accurate reconstruction of neuronal morphology (fMOST). These domain-
³⁷² informed assessments, also used in prior large-scale mapping projects⁴⁶, prioritize task-relevant

373 accuracy over other possible benchmarks such as Dice coefficients or landmark distances.

374 While formal quantitative scores were not reported for these specific pipelines, they both
375 demonstrate reliable, expert-validated performance in collaborative contexts. Additional
376 documentation and evaluation commentary are available in the updated CCFAAlignmentToolkit
377 GitHub repository.

378 For developmental data, we introduced a velocity field-based model for continuous interpo-
379 lation between discrete DevCCF timepoints. Although the DevCCF substantially expands
380 coverage of developmental stages relative to prior atlases, temporal gaps remain. The velocity
381 model enables spatio-temporal transformations within the full developmental interval and
382 supports the generation of virtual templates at unsampled ages. This functionality is built
383 using ANTsX components for velocity field optimization and integration, and offers a novel
384 mechanism for interpolating across the non-linear developmental trajectory of the mouse brain.
385 Such interpolation has potential utility for both anatomical harmonization and longitudinal
386 analyses. Interestingly, long-range transformations (e.g., P56 to E11.5) revealed anatomy
387 evolving in plausible ways yet sometimes diverging from known developmental patterns (e.g.,
388 hippocampal shape changes) reflecting the input data and offering insight into temporal gaps.
389 These behaviors could assist future efforts to determine which additional time points would
390 most improve spatiotemporal coverage.

391 We also introduced a template-based deep learning pipeline for mouse brain extraction and
392 parcellation using aggressive data augmentation. This approach is designed to reduce the
393 reliance on large annotated training datasets, which remain limited in the mouse imaging
394 domain. Evaluation on independent data demonstrates promising generalization, though
395 further refinement will be necessary. As with our human-based ANTsX pipelines, failure
396 cases can be manually corrected and recycled into future training cycles. Community
397 contributions are welcomed and encouraged, providing a pathway for continuous improvement
398 and adaptation to new datasets.

399 The ANTsX ecosystem offers a powerful foundation for constructing scalable, reproducible
400 pipelines for mouse brain data analysis. Its modular design and multi-platform support enable
401 researchers to develop customized workflows without extensive new software development.

⁴⁰² The widespread use of ANTsX components across the neuroimaging community attests to its
⁴⁰³ utility and reliability. As a continuation of the BICCN program, ANTsX is well positioned to
⁴⁰⁴ support the goals of the BRAIN Initiative Cell Atlas Network (BICAN) and future efforts to
⁴⁰⁵ extend these mapping strategies to the human brain.

406 **4 Methods**

407 The following methods are all available as part of the ANTsX ecosystem with analogous
408 elements existing in both ANTsR (ANTs in R) and ANTsPy (ANTs in Python), underpinned by
409 a shared ANTs/ITK C++ core. Most development for the work described was performed using
410 ANTsPy. For equivalent functionality in ANTsR, we refer the reader to the comprehensive
411 ANTsX tutorial: <https://tinyurl.com/antsxtutorial>.

412 **4.1 General ANTsX utilities**

413 Although focused on distinct data types, the three pipelines presented in this work share
414 common components that address general challenges in mapping mouse brain data. These
415 include correcting image intensity artifacts, denoising, spatial registration, template generation,
416 and visualization. Table 1 provides a concise summary of the relevant ANTsX functionality.

417 **Preprocessing: bias field correction and denoising.** Standard preprocessing steps in
418 mouse brain imaging include correcting for spatial intensity inhomogeneities and reducing
419 image noise, both of which can impact registration accuracy and downstream analysis. ANTsX
420 provides implementations of widely used methods for these tasks. The N4 bias field correction
421 algorithm⁵¹, originally developed in ANTs and contributed to ITK, mitigates artifactual, low-
422 frequency intensity variation and is accessible via `ants.n4_bias_field_correction(...)`.
423 Patch-based denoising⁶⁰ has been implemented as `ants.denoise_image(...)`.

424 **Image registration.** ANTsX includes a robust and flexible framework for pairwise
425 and groupwise image registration⁸⁰. At its core is the SyN algorithm⁵⁰, a symmetric
426 diffeomorphic model with optional B-spline regularization⁶⁶. In ANTsPy, registration
427 is performed via `ants.registration(...)` using preconfigured parameter sets (e.g.,
428 `antsRegistrationSyNQuick[s]`, `antsRegistrationSyN[s]`) suitable for different imaging
429 modalities and levels of computational demand. Resulting transformations can be applied to
430 new images with `ants.apply_transforms(...)`.

431 **Template generation.** ANTsX supports population-based template generation through
432 iterative pairwise registration to an evolving estimate of the mean shape and intensity

433 reference space across subjects⁵⁸. This functionality was used in generating the DevCCF
434 templates¹⁶. The procedure, implemented as `ants.build_template(...)`, produces average
435 images in both shape and intensity by aligning all inputs to a common evolving template.

436 **Visualization.** To support visual inspection and quality control, ANTsPy provides flexible
437 image visualization with `ants.plot(...)`. This function enables multi-slice and multi-
438 orientation rendering with optional overlays and label maps.

439 4.2 Mapping fMOST data to AllenCCFv3

440 **Preprocessing.** Mapping fMOST data into the AllenCCFv3 presents unique challenges due
441 to its native ultra-high resolution and imaging artifacts common to the fMOST modality.
442 Each fMOST image can exceed a terabyte in size, with spatial resolutions far exceeding
443 those of the AllenCCFv3 ($25\ \mu m$ isotropic). To reduce computational burden and prevent
444 resolution mismatch, each fMOST image is downsampled using cubic B-spline interpolation
445 via `ants.resample_image(...)` to match the template resolution.

446 Stripe artifacts (i.e., periodic intensity distortions caused by nonuniform sectioning or illumina-
447 nation) are common in fMOST and can mislead deformable registration algorithms. These
448 were removed using a custom 3D notch filter (`remove_stripe_artifact(...)`) implemented
449 in the `CCFAlignmentToolkit` using SciPy frequency domain filtering. The filter targets
450 dominant stripe frequencies along a user-specified axis in the Fourier domain. In addition,
451 intensity inhomogeneity across sections, often arising from variable staining or illumination,
452 was corrected using N4 bias field correction.

453 **Template-based spatial normalization.** To facilitate reproducible mapping, we first
454 constructed a contralaterally symmetric average template from 30 fMOST brains and their
455 mirrored counterparts using ANTsX template-building tools. Because the AllenCCFv3 and
456 fMOST data differ substantially in both intensity contrast and morphology, direct deformable
457 registration between individual fMOST brains and the AllenCCFv3 was insufficiently robust.
458 Instead, we performed a one-time expert-guided label-driven registration between the average
459 fMOST template and AllenCCFv3. This involved sequential alignment of seven manually

460 selected anatomical regions: 1) brain mask/ventricles, 2) caudate/putamen, 3) fimbria, 4)
461 posterior choroid plexus, 5) optic chiasm, 6) anterior choroid plexus, and 7) habenular com-
462 missure which were prioritized to enable coarse-to-fine correction of shape differences. Once
463 established, this fMOST-template-to-AllenCCFv3 transform was reused for all subsequent
464 specimens. Each new fMOST brain was then registered to the average fMOST template
465 using intensity-based registration, followed by concatenation of transforms to produce the
466 final mapping into AllenCCFv3 space.

467 **Mapping neuron projections.** A key advantage of fMOST imaging is its ability to
468 support single neuron projection reconstruction across the entire brain⁷⁷. Because these
469 reconstructions are stored as 3D point sets aligned to the original fMOST volume, we applied
470 the same composite transform used for image alignment to the point data using ANTsX
471 functionality. This enables seamless integration of cellular morphology data into AllenCCFv3
472 space, facilitating comparative analyses across specimens.

473 4.3 Mapping MERFISH data to AllenCCFv3

474 **Preprocessing.** MERFISH data are acquired as a series of 2D tissue sections, each comprising
475 spatially localized gene expression measurements at subcellular resolution. To enable 3D
476 mapping to the AllenCCFv3, we first constructed anatomical reference images by aggregating
477 the number of detected transcripts per voxel across all probes within each section. These 2D
478 projections were resampled to a resolution of $10 \mu m \times 10 \mu m$ to match the in-plane resolution
479 of the AllenCCFv3.

480 Sections were coarsely aligned using manually annotated dorsal and ventral midline points,
481 allowing initial volumetric reconstruction. However, anatomical fidelity remained limited by
482 variation in section orientation, spacing, and tissue loss. To further constrain alignment and
483 enable deformable registration, we derived region-level anatomical labels directly from the
484 gene expression data.

485 **Label creation.** To assign region labels to the MERFISH data, we use a cell type clustering
486 approach previously detailed⁴⁶. In short, manually dissected scRNASeq data was used

487 to establish the distribution of cell types present in each of the following major regions:
488 cerebellum, CTXsp, hindbrain, HPF, hypothalamus, isocortex, LSX, midbrain, OLF, PAL,
489 sAMY, STRd, STRv, thalamus and hindbrain. Clusters in the scRNA-seq dataset were then
490 used to assign similar clusters of cell types in the MERFISH data to the regions they are
491 predominantly found in the scRNA-seq data. To account for clusters that were found at
492 low frequency in regions outside its main region we calculated for each cell its 50 nearest
493 neighbors in physical space and reassigned each cell to the region annotation dominating its
494 neighborhood.

495 **Section matching via global alignment.** A major challenge was compensating for oblique
496 cutting angles and non-uniform section thickness, which distort the anatomical shape and
497 spacing of the reconstructed volume. Rather than directly warping the MERFISH data into
498 atlas space, we globally aligned the AllenCCFv3 to the MERFISH coordinate system. This
499 was done via an affine transformation followed by resampling of AllenCCFv3 sections to match
500 the number and orientation of MERFISH sections. This approach minimizes interpolation
501 artifacts in the MERFISH data and facilitates one-to-one section matching.

502 **Landmark-driven deformable alignment.** We used a 2.5D approach for fine alignment of
503 individual sections. In each MERFISH slice, deformable registration was driven by sequential
504 alignment of anatomical landmarks between the label maps derived from MERFISH and
505 AllenCCFv3. A total of nine regions, including isocortical layers 2/3, 5, and 6, the striatum,
506 hippocampus, thalamus, and medial/lateral habenula, were registered in an empirically
507 determined order. After each round, anatomical alignment was visually assessed by an expert,
508 and the next structure was selected to maximize improvement in the remaining misaligned
509 regions.

510 The final transform for each section combined the global affine alignment and the per-structure
511 deformable registrations. These were concatenated to generate a 3D mapping from the original
512 MERFISH space to the AllenCCFv3 coordinate system. Once established, the composite
513 mapping enables direct transfer of gene-level and cell-type data from MERFISH into atlas
514 space, allowing integration with other imaging and annotation datasets.

515 **4.4 DevCCF velocity flow transformation model**

516 The Developmental Common Coordinate Framework (DevCCF)¹⁶ provides a discrete set of
517 age-specific templates that temporally sample the developmental trajectory. To model this
518 biological progression more continuously, we introduce a velocity flow-based paradigm for
519 inferring diffeomorphic transformations between developmental stages. This enables anatom-
520 ically plausible estimation of intermediate templates or mappings at arbitrary timepoints
521 between the E11.5 and P56 endpoints of the DevCCF. Our approach builds on established
522 insights from time-varying diffeomorphic registration⁶⁵, where a velocity field governs the
523 smooth deformation of anatomical structures over time. Importantly, the framework is
524 extensible and can naturally accommodate additional timepoints for the potential expansion
525 of the DevCCF.

526 **Point sampling and region correspondence.** We first coalesced the anatomical labels
527 across the seven DevCCF templates (E11.5, E13.5, E15.5, E18.5, P4, P14, P56) into 26
528 common structures that could be consistently identified across development. These include
529 major brain regions such as the cortex, cerebellum, hippocampus, midbrain, and ventricles.
530 For each successive pair of templates, we performed multi-label deformable registration
531 using ANTsX to generate forward and inverse transforms between anatomical label volumes.
532 From the P56 space, we randomly sampled approximately 1e6 points within and along the
533 boundaries of each labeled region and propagated them through each pairwise mapping step
534 (e.g., P56 → P14, P14 → P4, ..., E13.5 → E11.5). This procedure created time-indexed
535 point sets tracing the spatial evolution of each region.

536 **Velocity field fitting.** Using these point sets, we fit a continuous velocity field over
537 developmental time using a generalized B-spline scattered data approximation method⁸⁶.
538 The field was parameterized over a log-scaled time axis to ensure finer temporal resolution
539 during early embryonic stages, where morphological changes are most rapid. Optimization
540 proceeded for approximately 125 iterations, minimizing the average Euclidean norm between
541 transformed points at each step. Ten integration points were used to ensure numerical
542 stability. The result is a smooth, differentiable vector field that defines a diffeomorphic
543 transform between any two timepoints within the template range.

544 **Applications and availability.** This velocity model can be used to estimate spatial transfor-
545 mations between any pair of developmental stages—even those for which no empirical template
546 exists—allowing researchers to create interpolated atlases, align new datasets, or measure con-
547 tinuous structural changes. It also enables developmental alignment of multi-modal data (e.g.,
548 MRI to LSFM) by acting as a unifying spatiotemporal scaffold. The underlying components
549 for velocity field fitting and integration are implemented in ITK, and the complete workflow
550 is accessible in both ANTsPy (`ants.fit_time_varying_transform_to_point_sets(...)`)
551 and ANTsR. In addition the availability of the DevCCF use case, self-contained examples
552 and usage tutorials are provided in our public codebase.

553 4.5 Automated brain extraction and parcellation with ANTsXNet

554 To support template-based deep learning approaches for structural brain extraction and par-
555 cellation, we implemented dedicated pipelines using the ANTsXNet framework. ANTsXNet
556 comprises open-source deep learning libraries in both Python (ANTsPyNet) and R (ANTsR-
557 Net) that interface with the broader ANTsX ecosystem and are built on TensorFlow/Keras.
558 Our mouse brain pipelines mirror existing ANTsXNet tools for human imaging but are
559 adapted for species-specific anatomical variation, lower SNR, and heterogeneous acquisition
560 protocols.

561 4.5.1 Deep learning training setup

562 All network-based approaches were implemented using a standard U-net⁸⁷ architecture and
563 hyperparameters previously evaluated in ANTsXNet pipelines for human brain imaging⁴⁵.
564 This design follows the ‘no-new-net’ principle⁸⁸, which demonstrates that a well-configured,
565 conventional U-net can achieve robust and competitive performance across a wide range
566 of biomedical segmentation tasks with little to no architectural modifications from the
567 original. Both networks use a 3D U-net architecture implemented in TensorFlow/Keras, with
568 five encoding/decoding levels and skip connections. The loss function combined Dice and
569 categorical cross-entropy terms. Training used a batch size of 4, Adam optimizer with an initial

learning rate of 2e-4, and early stopping based on validation loss. Training was performed on an NVIDIA DGX system ($4 \times$ Tesla V100 GPUs, 256 GB RAM). Model weights and preprocessing routines are shared across ANTsPyNet and ANTsRNet to ensure reproducibility and language portability. For both published and unpublished trained networks available through ANTsXNet, all training scripts and data augmentation generators are publicly available at <https://github.com/ntustison/ANTsXNetTraining>.

Data augmentation. Robust data augmentation was critical to generalization across scanners, contrast types, and resolutions. We applied both intensity- and shape-based augmentation strategies:

• *Intensity augmentations:*

- Gaussian, Poisson, and salt-and-pepper noise:
`ants.add_noise_to_image(...)`
- Simulated intensity inhomogeneity via bias field modeling⁵¹:
`antspynet.simulate_bias_field(...)`
- Histogram warping to simulate contrast variation⁸⁹:
`antspynet.histogram_warp_image_intensities(...)`

• *Shape augmentations:*

- Random nonlinear deformations and affine transforms:
`antspynet.randomly_transform_image_data(...)`
- Anisotropic resampling across axial, sagittal, and coronal planes:
`ants.resample_image(...)`

4.5.2 Brain extraction

We originally trained a mouse-specific brain extraction model on two manually masked T2-weighted templates, generated from public datasets^{67,68}. One of the templates was constructed from orthogonal 2D acquisitions using B-spline-based volumetric synthesis

595 via `ants.fit_bspline_object_to_scattered_data(...)`. Normalized gradient magnitude
596 was used as a weighting function to emphasize boundaries during reconstruction⁸⁶.

597 This training strategy provides strong spatial priors despite limited data by leveraging
598 high-quality template images and aggressive augmentation to mimic population variability.
599 During the development of this work, the network was further refined through community
600 engagement. A user from a U.S.-based research institute applied this publicly available (but
601 then unpublished) brain extraction tool to their own mouse MRI dataset. Based on feedback
602 and iterative collaboration with the ANTsX team, the model was retrained and improved to
603 better generalize to additional imaging contexts. This reflects our broader commitment to
604 community-driven development and responsiveness to user needs across diverse mouse brain
605 imaging scenarios.

606 The final trained network is available via ANTsXNet through the function
607 `antspynet.mouse_extraction(...)`. Additionally, both template/mask pairs are
608 accessible via ANTsXNet. For example, one such image pair is available via:

- Template:

```
antspynet.get_antsxnet_data("bsplineT2MouseTemplate")
```

- Brain mask:

```
antspynet.get_antsxnet_data("bsplineT2MouseTemplateBrainMask")
```

613 4.5.3 Brain parcellation

614 For brain parcellation, we trained a 3D U-net model using the DevCCF P56 T2-weighted
615 template and anatomical segmentations derived from AllenCCFv3. This template-based
616 training strategy enables the model to produce accurate, multi-region parcellations without
617 requiring large-scale annotated subject data.

618 To normalize intensity across specimens, input images were preprocessed using rank-based
619 intensity normalization (`ants.rank_intensity(...)`). Spatial harmonization was achieved
620 through affine and deformable alignment of each extracted brain to the P56 template prior

621 to inference. In addition to the normalized image input, the network also receives prior
622 probability maps derived from the atlas segmentations, providing additional spatial context.

623 This general parcellation deep learning framework has also been applied in collaboration
624 with other groups pursuing related but distinct projects. In one case, a model variant
625 was adapted for T2-weighted MRI using an alternative anatomical labeling scheme; in
626 another, a separate model was developed for serial two-photon tomography (STPT) with
627 a different parcellation set. All three models are accessible through a shared interface
628 in ANTsXNet: `antspynet.mouse_brain_parcellation(...)`. Ongoing work is further
629 extending this approach to embryonic mouse brain data. These independent efforts reflect
630 broader community interest in adaptable parcellation tools and reinforce the utility of
631 ANTsXNet as a platform for reproducible, extensible deep learning workflows.

632 4.5.4 Evaluation and reuse

633 To assess model generalizability, both the brain extraction and parcellation networks were
634 evaluated on an independent longitudinal dataset comprising multiple imaging sessions
635 with varied acquisition parameters⁶⁹. Although each label or imaging modality required
636 retraining, the process was streamlined by the reusable ANTsX infrastructure enabled by
637 rapid adaptation with minimal overhead. These results illustrate the practical benefits of a
638 template-based, low-shot strategy and modular deep learning framework. All trained models,
639 associated training scripts, and supporting resources are openly available and designed for
640 straightforward integration into ANTsX workflows.

641 **Data Availability**

642 The following datasets were used in this study and are publicly available:

- 643 • **Allen Common Coordinate Framework (AllenCCFv3):** Available from the Allen
644 Institute for Brain Science at <https://atlas.brain-map.org/atlas>.
- 645 • **Developmental Common Coordinate Framework (DevCCF) MRI and LSFM**
646 datasets: Publicly available via the Kim Lab <https://kimlab.io/home/projects/>
647 [DevCCF/index.html](#).
- 648 • **MERFISH spatial transcriptomics data:** Previously published⁴⁶ [https://portal.](https://portal.brain-map.org)
649 [brain-map.org](#).
- 650 • **Developmental datasets for brain extraction and segmentation:**
 - 651 – High-resolution MRI data of brain C57BL/6 and BTBR mice in three different
652 anatomical views: <https://data.mendeley.com/datasets/dz9x23fttt/1>.
 - 653 – CAMRI Mouse Brain Data: <https://openneuro.org/datasets/ds002868/versions/1.0.1>
- 655 • **Evaluation dataset for brain extraction and segmentation:** A longitudinal
656 microstructural MRI dataset in healthy C57Bl/6 mice at 9.4 Tesla <https://www.frdr-dfdr.ca/repo/dataset/9ea832ad-7f36-4e37-b7ac-47167c0001c1>.
- 658 • **ANTsXNet-pretrained templates and models:** Available through ANTsPy at
659 <https://github.com/ANTsX/ANTsPyNet>.

660 **Code Availability**

661 All processing pipelines and supporting code are openly available at:

- 662 • <https://github.com/ntustison/ANTsXMouseBrainMapping> (DevCCF velocity model
663 and deep learning parcellation). Also contains the text, scripts, and data to reproduce
664 the manuscript (including figures).
- 665 • <https://github.com/dontminchenit/CCFAlignmentToolkit> (MERFISH and fMOST
666 workflows)

667 **References**

- 668 1. Keller, P. J. & Ahrens, M. B. Visualizing whole-brain activity and development at the
single-cell level using light-sheet microscopy. *Neuron* **85**, 462–83 (2015).
- 669 2. La Manno, G. *et al.* Molecular architecture of the developing mouse brain. *Nature*
596, 92–96 (2021).
- 670 3. Wen, L. *et al.* Single-cell technologies: From research to application. *Innovation
(Camb)* **3**, 100342 (2022).
- 671 4. Oh, S. W. *et al.* A mesoscale connectome of the mouse brain. *Nature* **508**, 207–14
(2014).
- 672 5. Gong, H. *et al.* Continuously tracing brain-wide long-distance axonal projections in
mice at a one-micron voxel resolution. *Neuroimage* **74**, 87–98 (2013).
- 673 6. Li, A. *et al.* Micro-optical sectioning tomography to obtain a high-resolution atlas of
the mouse brain. *Science* **330**, 1404–8 (2010).
- 674 7. Ueda, H. R. *et al.* Tissue clearing and its applications in neuroscience. *Nat Rev
Neurosci* **21**, 61–79 (2020).
- 675 8. Ståhl, P. L. *et al.* Visualization and analysis of gene expression in tissue sections by
spatial transcriptomics. *Science* **353**, 78–82 (2016).
- 676 9. Burgess, D. J. Spatial transcriptomics coming of age. *Nat Rev Genet* **20**, 317 (2019).
- 677 10. Hardwick, S. A. *et al.* Single-nuclei isoform RNA sequencing unlocks barcoded exon
connectivity in frozen brain tissue. *Nature biotechnology* **40**, 1082–1092 (2022).
- 678 11. Hawrylycz, M. *et al.* A guide to the BRAIN initiative cell census network data
ecosystem. *PLoS biology* **21**, e3002133 (2023).
- 679 12. Wang, Q. *et al.* The allen mouse brain common coordinate framework: A 3D reference
atlas. *Cell* **181**, 936–953.e20 (2020).
- 680 13. Perens, J. *et al.* An optimized mouse brain atlas for automated mapping and quantifi-
cation of neuronal activity using iDISCO+ and light sheet fluorescence microscopy.
Neuroinformatics **19**, 433–446 (2021).
- 681 14. Ma, Y. *et al.* A three-dimensional digital atlas database of the adult C57BL/6J mouse
brain by magnetic resonance microscopy. *Neuroscience* **135**, 1203–1215 (2005).

- 682 15. Qu, L. *et al.* Cross-modal coherent registration of whole mouse brains. *Nature Methods* **19**, 111–118 (2022).
- 683 16. Kronman, F. N. *et al.* [Developmental mouse brain common coordinate framework](#). *Nat Commun* **15**, 9072 (2024).
- 684 17. Chuang, N. *et al.* An MRI-based atlas and database of the developing mouse brain. *Neuroimage* **54**, 80–89 (2011).
- 685 18. Dries, R. *et al.* Advances in spatial transcriptomic data analysis. *Genome research* **31**, 1706–1718 (2021).
- 686 19. Ricci, P. *et al.* Removing striping artifacts in light-sheet fluorescence microscopy: A review. *Progress in biophysics and molecular biology* **168**, 52–65 (2022).
- 687 20. Agarwal, N., Xu, X. & Gopi, M. Robust registration of mouse brain slices with severe histological artifacts. in *Proceedings of the tenth indian conference on computer vision, graphics and image processing* 1–8 (2016).
- 688 21. Agarwal, N., Xu, X. & Gopi, M. Automatic detection of histological artifacts in mouse brain slice images. in *Medical computer vision and bayesian and graphical models for biomedical imaging: MICCAI 2016 international workshops, MCV and BAMBI, athens, greece, october 21, 2016, revised selected papers* 8 105–115 (Springer, 2017).
- 689 22. Tward, D. *et al.* 3d mapping of serial histology sections with anomalies using a novel robust deformable registration algorithm. in *International workshop on multimodal brain image analysis* 162–173 (Springer, 2019).
- 690 23. Cahill, L. S. *et al.* Preparation of fixed mouse brains for MRI. *Neuroimage* **60**, 933–939 (2012).
- 691 24. Biancalani, T. *et al.* [Deep learning and alignment of spatially resolved single-cell transcriptomes with tangram](#). *Nat Methods* **18**, 1352–1362 (2021).
- 692 25. Sunkin, S. M. *et al.* Allen brain atlas: An integrated spatio-temporal portal for exploring the central nervous system. *Nucleic acids research* **41**, D996–D1008 (2012).
- 693 26. Kim, Y. *et al.* Brain-wide maps reveal stereotyped cell-type-based cortical architecture and subcortical sexual dimorphism. *Cell* **171**, 456–469 (2017).

- 694 27. Fürth, D. *et al.* An interactive framework for whole-brain maps at cellular resolution. *Nat Neurosci* **21**, 139–149 (2018).
- 695 28. Li, Y. *et al.* mBrainAligner-web: A web server for cross-modal coherent registration of whole mouse brains. *Bioinformatics* **38**, 4654–4655 (2022).
- 696 29. Puchades, M. A., Csucs, G., Ledergerber, D., Leergaard, T. B. & Bjaalie, J. G. Spatial registration of serial microscopic brain images to three-dimensional reference atlases with the QuickNII tool. *PLoS one* **14**, e0216796 (2019).
- 697 30. Eastwood, B. S. *et al.* Whole mouse brain reconstruction and registration to a reference atlas with standard histochemical processing of coronal sections. *Journal of Comparative Neurology* **527**, 2170–2178 (2019).
- 698 31. Ni, H. *et al.* A robust image registration interface for large volume brain atlas. *Sci Rep* **10**, 2139 (2020).
- 699 32. Pallast, N. *et al.* Processing pipeline for atlas-based imaging data analysis of structural and functional mouse brain MRI (AIDAmri). *Front Neuroinform* **13**, 42 (2019).
- 700 33. Celestine, M., Nadkarni, N. A., Garin, C. M., Bougacha, S. & Dhenain, M. **Sammba-MRI: A library for processing SmAll-MaMmal BrAin MRI data in python**. *Front Neuroinform* **14**, 24 (2020).
- 701 34. Ioanas, H.-I., Marks, M., Zerbi, V., Yanik, M. F. & Rudin, M. An optimized registration workflow and standard geometric space for small animal brain imaging. *Neuroimage* **241**, 118386 (2021).
- 702 35. Aggarwal, M., Zhang, J., Miller, M. I., Sidman, R. L. & Mori, S. Magnetic resonance imaging and micro-computed tomography combined atlas of developing and adult mouse brains for stereotaxic surgery. *Neuroscience* **162**, 1339–1350 (2009).
- 703 36. Chandrashekhar, V. *et al.* CloudReg: Automatic terabyte-scale cross-modal brain volume registration. *Nature methods* **18**, 845–846 (2021).
- 704 37. Jin, M. *et al.* SMART: An open-source extension of WholeBrain for intact mouse brain registration and segmentation. *eNeuro* **9**, (2022).
- 705 38. Negwer, M. *et al.* FriendlyClearMap: An optimized toolkit for mouse brain mapping and analysis. *Gigascience* **12**, (2022).

- 706 39. Lin, W. *et al.* Whole-brain mapping of histaminergic projections in mouse brain. *Proceedings of the National Academy of Sciences* **120**, e2216231120 (2023).
- 707 40. Zhang, M. *et al.* Spatially resolved cell atlas of the mouse primary motor cortex by MERFISH. *Nature* **598**, 137–143 (2021).
- 708 41. Shi, H. *et al.* Spatial atlas of the mouse central nervous system at molecular resolution. *Nature* **622**, 552–561 (2023).
- 709 42. Zhang, Y. *et al.* Reference-based cell type matching of *in situ* image-based spatial transcriptomics data on primary visual cortex of mouse brain. *Scientific Reports* **13**, 9567 (2023).
- 710 43. Klein, S., Staring, M., Murphy, K., Viergever, M. A. & Pluim, J. P. W. [Elastix: A toolbox for intensity-based medical image registration](#). *IEEE Trans Med Imaging* **29**, 196–205 (2010).
- 711 44. Fedorov, A. *et al.* 3D slicer as an image computing platform for the quantitative imaging network. *Magnetic resonance imaging* **30**, 1323–1341 (2012).
- 712 45. Tustison, N. J. *et al.* [The ANTsX ecosystem for quantitative biological and medical imaging](#). *Sci Rep* **11**, 9068 (2021).
- 713 46. Yao, Z. *et al.* [A high-resolution transcriptomic and spatial atlas of cell types in the whole mouse brain](#). *Nature* **624**, 317–332 (2023).
- 714 47. Pagani, M., Damiano, M., Galbusera, A., Tsafaris, S. A. & Gozzi, A. Semi-automated registration-based anatomical labelling, voxel based morphometry and cortical thickness mapping of the mouse brain. *Journal of neuroscience methods* **267**, 62–73 (2016).
- 715 48. Anderson, R. J. *et al.* [Small animal multivariate brain analysis \(SAMBA\) - a high throughput pipeline with a validation framework](#). *Neuroinformatics* **17**, 451–472 (2019).
- 716 49. Allan Johnson, G. *et al.* Whole mouse brain connectomics. *Journal of Comparative Neurology* **527**, 2146–2157 (2019).

- 717 50. Avants, B. B., Epstein, C. L., Grossman, M. & Gee, J. C. [Symmetric diffeomorphic](#)
image registration with cross-correlation: Evaluating automated labeling of elderly
and neurodegenerative brain. *Med Image Anal* **12**, 26–41 (2008).
- 718 51. Tustison, N. J. *et al.* [N4ITK: Improved N3 bias correction](#). *IEEE Trans Med Imaging*
29, 1310–20 (2010).
- 719 52. Bajcsy, R. & Broit, C. Matching of deformed images. in *Sixth International Conference*
on Pattern Recognition (ICPR'82) 351–353 (1982).
- 720 53. Bajcsy, R. & Kovacic, S. [Multiresolution elastic matching](#). *Computer Vision, Graphics,*
and Image Processing **46**, 1–21 (1989).
- 721 54. Gee, J. C., Reivich, M. & Bajcsy, R. [Elastically deforming 3D atlas to match anatomical](#)
[brain images](#). *J Comput Assist Tomogr* **17**, 225–36 (1993).
- 722 55. Klein, A. *et al.* [Evaluation of 14 nonlinear deformation algorithms applied to human](#)
[brain MRI registration](#). *Neuroimage* **46**, 786–802 (2009).
- 723 56. Murphy, K. *et al.* [Evaluation of registration methods on thoracic CT: The EMPIRE10](#)
[challenge](#). *IEEE Trans Med Imaging* **30**, 1901–20 (2011).
- 724 57. Baheti, B. *et al.* [The brain tumor sequence registration challenge: Establishing](#)
correspondence between pre-operative and follow-up MRI scans of diffuse glioma
patients. (2021).
- 725 58. Avants, B. B. *et al.* [The optimal template effect in hippocampus studies of diseased](#)
[populations](#). *Neuroimage* **49**, 2457–66 (2010).
- 726 59. Avants, B. B., Tustison, N. J., Wu, J., Cook, P. A. & Gee, J. C. [An open source](#)
[multivariate framework for n-tissue segmentation with evaluation on public data](#).
Neuroinformatics **9**, 381–400 (2011).
- 727 60. Manjón, J. V., Coupé, P., Martí-Bonmatí, L., Collins, D. L. & Robles, M. [Adaptive](#)
[non-local means denoising of MR images with spatially varying noise levels](#). *J Magn*
Reson Imaging **31**, 192–203 (2010).
- 728 61. Wang, H. *et al.* [Multi-atlas segmentation with joint label fusion](#). *IEEE Trans Pattern*
Anal Mach Intell **35**, 611–23 (2013).

- 729 62. Tustison, N. J. *et al.* Optimal symmetric multimodal templates and concatenated random forests for supervised brain tumor segmentation (simplified) with *ANTsR*. *Neuroinformatics* (2014) doi:10.1007/s12021-014-9245-2.
- 730 63. Tustison, N. J., Yang, Y. & Salerno, M. Advanced normalization tools for cardiac motion correction. in *Statistical atlases and computational models of the heart - imaging and modelling challenges* (eds. Camara, O. et al.) vol. 8896 3–12 (Springer International Publishing, 2015).
- 731 64. McCormick, M., Liu, X., Jomier, J., Marion, C. & Ibanez, L. ITK: Enabling reproducible research and open science. *Front Neuroinform* **8**, 13 (2014).
- 732 65. Beg, M. F., Miller, M. I., Trouvé, A. & Younes, L. Computing large deformation metric mappings via geodesic flows of diffeomorphisms. *International Journal of Computer Vision* **61**, 139–157 (2005).
- 733 66. Tustison, N. J. & Avants, B. B. Explicit B-spline regularization in diffeomorphic image registration. *Front Neuroinform* **7**, 39 (2013).
- 734 67. Hsu, L.-M. *et al.* CAMRI mouse brain MRI data.
- 735 68. Reshetnikov, V. *et al.* High-resolution MRI data of brain C57BL/6 and BTBR mice in three different anatomical views.
- 736 69. Rahman, N., Xu, K., Budde, M. D., Brown, A. & Baron, C. A. A longitudinal microstructural MRI dataset in healthy C57Bl/6 mice at 9.4 tesla. *Sci Data* **10**, 94 (2023).
- 737 70. Liu, J. *et al.* Concordance of MERFISH spatial transcriptomics with bulk and single-cell RNA sequencing. *Life Sci Alliance* **6**, (2023).
- 738 71. Stringer, C., Wang, T., Michaelos, M. & Pachitariu, M. Cellpose: A generalist algorithm for cellular segmentation. *Nat Methods* **18**, 100–106 (2021).
- 739 72. Jia, H., Yap, P.-T., Wu, G., Wang, Q. & Shen, D. Intermediate templates guided groupwise registration of diffusion tensor images. *NeuroImage* **54**, 928–939 (2011).
- 740 73. Tang, S., Fan, Y., Wu, G., Kim, M. & Shen, D. RABBIT: Rapid alignment of brains by building intermediate templates. *NeuroImage* **47**, 1277–1287 (2009).

- 741 74. Dewey, B. E., Carass, A., Blitz, A. M. & Prince, J. L. Efficient multi-atlas registration
using an intermediate template image. in *Proceedings of SPIE—the international society
for optical engineering* vol. 10137 (NIH Public Access, 2017).
- 742 75. Perens, J. *et al.* Multimodal 3D mouse brain atlas framework with the skull-derived
coordinate system. *Neuroinformatics* **21**, 269–286 (2023).
- 743 76. Rotolo, T., Smallwood, P. M., Williams, J. & Nathans, J. Genetically-directed, cell
type-specific sparse labeling for the analysis of neuronal morphology. *PLoS One* **3**,
e4099 (2008).
- 744 77. Peng, H. *et al.* Morphological diversity of single neurons in molecularly defined cell
types. *Nature* **598**, 174–181 (2021).
- 745 78. Gong, H. *et al.* High-throughput dual-colour precision imaging for brain-wide connec-
tome with cytoarchitectonic landmarks at the cellular level. *Nat Commun* **7**, 12142
(2016).
- 746 79. Wang, J. *et al.* Divergent projection patterns revealed by reconstruction of individual
neurons in orbitofrontal cortex. *Neurosci Bull* **37**, 461–477 (2021).
- 747 80. Avants, B. B. *et al.* The Insight ToolKit image registration framework. *Front Neu-
roinform* **8**, 44 (2014).
- 748 81. Chon, U., Vanselow, D. J., Cheng, K. C. & Kim, Y. Enhanced and unified anatomical
labeling for a common mouse brain atlas. *Nat Commun* **10**, 5067 (2019).
- 749 82. Tasic, B. *et al.* Adult mouse cortical cell taxonomy revealed by single cell transcript-
omics. *Nat Neurosci* **19**, 335–46 (2016).
- 750 83. Bergmann, E., Gofman, X., Kavushansky, A. & Kahn, I. Individual variability in
functional connectivity architecture of the mouse brain. *Commun Biol* **3**, 738 (2020).
- 751 84. Billot, B. *et al.* SynthSeg: Segmentation of brain MRI scans of any contrast and
resolution without retraining. *Med Image Anal* **86**, 102789 (2023).
- 752 85. Rolfe, S. M., Whikehart, S. M. & Maga, A. M. Deep learning enabled multi-organ
segmentation of mouse embryos. *Biol Open* **12**, bio059698 (2023).

- 753 86. Tustison, N. J. & Gee, J. C. Generalized n -d C^k B-spline scattered data approximation
with confidence values. in *Medical imaging and augmented reality* (eds. Yang, G.-Z.,
Jiang, T., Shen, D., Gu, L. & Yang, J.) 76–83 (Springer Berlin Heidelberg, 2006).
- 754 87. Falk, T. *et al.* U-net: Deep learning for cell counting, detection, and morphometry.
Nat Methods **16**, 67–70 (2019).
- 755 88. Isensee, F., Jaeger, P. F., Kohl, S. A. A., Petersen, J. & Maier-Hein, K. H. nnU-net: A
self-configuring method for deep learning-based biomedical image segmentation. *Nat
Methods* **18**, 203–211 (2021).
- 756 89. Tustison, N. J. *et al.* Image- versus histogram-based considerations in semantic
segmentation of pulmonary hyperpolarized gas images. *Magn Reson Med* **86**, 2822–2836
(2021).

⁷⁵⁷ **Acknowledgments**

⁷⁵⁸ Support for the research reported in this work includes funding from the National Institute
⁷⁵⁹ of Biomedical Imaging and Bioengineering (R01-EB031722) and National Institute of Mental
⁷⁶⁰ Health (RF1-MH124605, U24-MH114827, and NIH RF1MH124605 to Y.K.).

⁷⁶¹ We also acknowledge the data contribution of Dr. Adam Raikes (GitHub @araikes) of the
⁷⁶² Center for Innovation in Brain Science at the University of Arizona for refining the weights
⁷⁶³ of the mouse brain extraction network.

⁷⁶⁴ **Author contributions**

⁷⁶⁵ N.T., M.C., and J.G. wrote the main manuscript text and figures. M.C., M.K., R.D., S.S.,
⁷⁶⁶ Q.W., L.G., J.D., C.G., and J.G. developed the Allen registration pipelines. N.T., F.K., J.G.,
⁷⁶⁷ and Y.K. developed the time-varying velocity transformation model for the DevCCF. N.T.
⁷⁶⁸ and M.T. developed the brain parcellation and cortical thickness methodology. All authors
⁷⁶⁹ reviewed the manuscript.

⁷⁷⁰ Competing Interests

⁷⁷¹ The authors declare no competing interests.

₇₇₂ **Tables**

Table 1: Sampling of ANTsX functionality

ANTsPy: Preprocessing	
bias field correction	<code>n4_bias_field_correction(...)</code>
image denoising	<code>denoise_image(...)</code>
ANTsPy: Registration	
intensity image registration	<code>registration(...)</code>
label image registration	<code>label_image_registration(...)</code>
image transformation	<code>apply_transforms(...)</code>
template generation	<code>build_template(...)</code>
landmark registration	<code>fit_transform_to_paired_points(...)</code>
time-varying landmark reg.	<code>fit_time_varying_transform_to_point_sets(...)</code>
integrate velocity field	<code>integrate_velocity_field(...)</code>
invert displacement field	<code>invert_displacement_field(...)</code>
ANTsPy: Segmentation	
MRF-based segmentation	<code>atropos(...)</code>
Joint label fusion	<code>joint_label_fusion(...)</code>
diffeomorphic thickness	<code>kelly_kapowski(...)</code>
ANTsPy: Miscellaneous	
Regional intensity statistics	<code>label_stats(...)</code>
Regional shape measures	<code>label_geometry_measures(...)</code>
B-spline approximation	<code>fit_bspline_object_to_scattered_data(...)</code>
Visualize images and overlays	<code>plot(...)</code>
<i>ANTsPyNet: Mouse-specific</i>	
brain extraction	<code>mouse_brain_extraction(...modality="t2"...)</code>
brain parcellation	<code>mouse_brain_parcellation(...)</code>
cortical thickness	<code>mouse_cortical_thickness(...)</code>
super resolution	<code>mouse_histology_super_resolution(...)</code>

ANTsX provides state-of-the-art functionality for processing biomedical image data. Such tools, including deep learning networks, support a variety of mapping-related tasks. A more comprehensive listing of ANTsX tools with self-contained R and Python examples is provided as a gist page on GitHub (<https://tinyurl.com/antsxtutorial>).

773 5 Figure Legends

774 **Figure 1.** Diagram of the two ANTsX-based pipelines for mapping (a) MERFISH and
775 (b)fMOST data into the space of AllenCCFv3. Each generates the requisite transforms to
776 map individual images to the CCF.

777 **Figure 2.** The spatial transformation between any two time points within the continuous
778 DevCCF longitudinal developmental trajectory is available through the use of ANTsX
779 functionality for generating a velocity flow model.

780 **Figure 3.** Annotated regions representing common labels across developmental stages, shown
781 for both P4 and P14.

782 **Figure 4.** Convergence and evaluation of the velocity flow model across the DevCCF develop-
783 mental trajectory. (Top left) Total displacement error over iterations. (Top right) Median
784 displacement error per integration point across the optimization timeline, spanning embryonic
785 (E11.5) to postnatal (P56) stages. (Bottom) Dice similarity scores comparing region-level
786 label overlap between: (1) conventional pairwise SyN registration and (2) velocity flow-based
787 deformation, across intermediate timepoints. Using region-based pairwise registration with
788 SyN as a performance upper bound, the velocity flow model achieves comparable accuracy
789 while also enabling smooth, continuous deformation across the full developmental continuum.

790 **Figure 5.** Mid-sagittal visualization of DevCCF templates warped to every other time point.
791 Each row is a reference space; each column is a warped input. Diagonal entries show original
792 templates.

793 **Figure 6.** Example of generating “virtual” DevCCF templates at intermediate time points
794 (e.g., P10.3, P20) by warping adjacent stages to a shared time and averaging using ANTsX.

795 **Figure 7.** The mouse brain cortical labeling pipeline integrates two deep learning components
796 for brain extraction and anatomical region segmentation. Both networks rely heavily on
797 data augmentation applied to templates constructed from open datasets. The framework
798 also supports further refinement or alternative label sets tailored to specific research needs.
799 Possible applications include voxelwise cortical thickness estimation.

800 **Figure 8.** Evaluation of the ANTsX mouse brain extraction on an independent, publicly
801 available dataset consisting of 12 specimens \times 7 time points = 84 total images. Dice overlap
802 comparisons with the user-generated brain masks provide good agreement with the automated
803 results from the brain extraction network.

804 **Figure 9.** Evaluation of the ANTsX deep learning-based mouse brain parcellation on a
805 diverse MRI cohort. (a) T2-weighted DevCCF P56 template with the six-region parcellation:
806 cerebral cortex, nuclei, brain stem, cerebellum, main olfactory bulb, and hippocampal
807 formation. (b) Example segmentation result from a representative subject (NR5, Day 0)
808 using the proposed deep learning pipeline. (c) Dice overlap scores across the full evaluation
809 cohort ($n = 84$), comparing anatomical alignment achieved via registration using intensity
810 alone versus registration guided by the predicted parcellation. Dice values were computed
811 using manually segmented labels transformed to AllenCCFv3 space.